IEEE Access
Multidisciplinary ⋮ Rapid Review ⋮ Open Access Journal

Received 21 March 2023, accepted 14 May 2023, date of publication 30 May 2023, date of current version 8 June 2023.

Digital Object Identifier 10.1109/ACCESS.2023.3281481

RESEARCH ARTICLE

Features and Properties of Single-Pixel Imaging Using Speckle Patterns Generated by Multi-Core Fiber

RYUTA YAMAGUCHI[1], **KANAMI IKEDA**[1,2], **OSANORI KOYAMA**[1,2], **(Member, IEEE), AND MAKOTO YAMADA**[1,2], **(Senior Member, IEEE)**

[1]Graduate School of Engineering, Osaka Prefecture University, Osaka 599-8531, Japan
[2]Graduate School of Engineering, Osaka Metropolitan University, Osaka 599-8531, Japan

Corresponding author: Kanami Ikeda (kanami@omu.ac.jp)

This work was supported in part by the Japan Society for the Promotion of Science (JSPS) KAKENHI under Grant JP19K15465 and Grant JP22K14619.

ABSTRACT Single-pixel imaging (SPI) has recently drawn considerable attention as a new imaging technique. An SPI system using a multi-core fiber (MCF-SPI system) that we proposed has the potential to make the system very compact. This study is concerned with the features and reconstruction properties of MCF-SPI system. In this system, the reconstruction quality varies widely depending on the number and placement of cores. It is necessary to use reconstruction algorithms suitable for the system, considering the performance limitations of the patterns, to improve the output reconstruction quality. The features and properties of speckle patterns generated by MCFs with different core layouts and algorithms were investigated to improve the reconstruction performance based on numerical simulation. Four existing algorithms were compared under several conditions to evaluate the algorithms that improve reconstruction quality. Compressive sensing based on total variation is the most compatible algorithm for MCF-SPI. It was confirmed that the MCF-SPI system performs well in terms of imaging quality if a suitable core layout and algorithm for the application are set.

INDEX TERMS Single-pixel imaging, multi-core fiber, image reconstruction, compressive sensing.

I. INTRODUCTION

Single-pixel imaging (SPI) is a technique that uses structured illumination (called patterns) and a single-pixel detector instead of a conventional 2D array sensor [1]. Reconstructed images can be obtained using illumination patterns sequentially modulated by a light modulator and the intensity of the reflected light from the target object. Because of its wide spectral range and high signal-to-noise ratio, SPI has been applied in various applications fields, such as multispectral imaging [2], [3], X-ray imaging [4], [5], terahertz imaging [6], [7], 3D imaging [8], [9], imaging in turbid water [10], [11], and optical encryption [12], [13].

Although general SPI systems employ spatial light modulators (SLMs) for pattern modulation, reducing the system size is challenging. To address this issue, SPI systems based on optical communication devices, such as multimode fibers (MMFs) [14], optical fiber phased arrays (OFPAs) [15], and multi-core fibers (MCFs) [16], have been proposed. An MCF is an optical fiber with multiple light waveguides (cores) in a cladding that has been actively studied for space-division multiplexing [17], [18]. The SPI system using an MCF (MCF-SPI system) generates patterns using an MCF and has been experimentally demonstrated using a seven-core fiber [19]. In MCF-SPI system, light output from multiple cores at the end face of an MCF produces speckle patterns by diffraction and interference of each light. In addition, the MCF may receive the light reflected from the target objects [20]. Because an MCF can perform both pattern generation and light reception, very compact systems with diameters of approximately 125–200 μm can be realized. In addition, the modulation of patterns generated by MCFs is several tens of gigahertz in theory, which is significantly faster than the frame rate of SLMs, up to several tens of

The associate editor coordinating the review of this manuscript and approving it for publication was Chao Zuo.

kilohertz owing to the high-speed modulation based on optical communication techniques. MCF-SPI systems are advantageous compared to other SPI systems based on optical fibers because they are more compact than those with OFPAs and have higher modulation speeds than those with MMFs.

Generally, the image quality of reconstructed images in SPI depends on the resolution of the patterns and the sampling number. To reconstruct the objects perfectly, high-resolution patterns are required to obtain detailed information about the objects with sufficient sampling numbers. However, in the MCF-SPI system, MCF patterns have limited complexity and variety owing to the limited number of cores placed in the cladding. Hence, the reconstruction quality varies widely depending on the number and placement of cores. Therefore, the reconstruction features and properties of speckle patterns generated by MCFs with different core layouts must be investigated. Furthermore, in order to improve the reconstruction quality of MCF-SPI, algorithms suitable for the system must also be identified considering the performance limitations of the patterns because in SPI, revising reconstruction algorithms for inverse problems improves the quality of the reconstructed images and reduces the calculation costs [21].

This study is concerned with the features and reconstruction properties of MCF-SPI system. We investigated the algorithms that improve the reconstruction performance of the system. Specifically, we prepared target objects and evaluated their compatibility with the existing reconstruction algorithms and objects. The results of this study provide new knowledge regarding SPI using speckle patterns. The remainder of this paper is organized as follows. Section II introduces MCF-SPI and the reconstruction algorithm methodology. Section III describes the simulation setup. Section IV presents the simulation results and a corresponding discussion. Finally, Section V summarizes the conclusions of the study.

II. METHODOLOGY

A. MCF-SPI

The light emitted by the light source is split and phase-modulated by the modulators. The split lights are then coupled to each core and emitted by the end face of the MCF. The spatial pattern, called the MCF pattern, is projected onto an object, and the pattern texture can be changed by phase modulation of the light in each core. The light intensity reflected by the object is received by a core of the MCF and detected by a single-pixel detector. The light intensity B_i detected by a single-pixel detector can be calculated by integrating the pattern $I_i(x, y)$ and object $T(x, y)$, written as

$$B_i = \int I_i(x, y)T(x, y)\mathrm{d}x\mathrm{d}y \tag{1}$$

where i is the number of pattern measurements. Using the patterns and detected light intensities, reconstructed images can be obtained by employing reconstruction algorithms.

B. RECONSTRUCTION ALGORITHMS

After M time measurements, we can obtain the linear equation

$$\boldsymbol{B} = \boldsymbol{IO}, \tag{2}$$

where $\boldsymbol{B} = [B_1, B_2, \cdots, B_M]^{\mathrm{T}}$ is the $M \times 1$ matrix representing the set of light intensities, $\boldsymbol{I} = [\boldsymbol{I_1}, \boldsymbol{I_2}, \cdots, \boldsymbol{I_M}]^{\mathrm{T}}$ is the $M \times N$ matrix (N is the number of pixels of patterns or the object) representing the set of illumination patterns, and $\boldsymbol{O}$ is the $N \times 1$ unknown matrix.

In this study, we applied four algorithms: compressive sensing (CS) based on the discrete cosine transform (DCT), CS based on total variation (TVCS), CS based on low-rank constraints (LRCS), and the iterative compressive (IC) method.

1) CS

CS is a technique for reconstructing signals with fewer measurements than the number of unknowns by introducing a sparse prior [22], [23]. To ensure the sparsity of natural images, the DCT, total variation (TV), and low-rank constraints were employed.

a: CS BASED ON DCT [24], [25]

The DCT expresses images in the frequency domain and is well known for JPEG compression. A large amount of information about natural images is stored in low-frequency components, and other frequencies exhibit sparsity. The DCT is the most common sparse expression in SPI reconstruction; therefore, we call this method CS. Specifically, using the DCT matrix $\boldsymbol{\phi}$, the reconstruction algorithm can be obtained by solving the following minimization problem consisting of l_2 and l_1 norms:

$$\min_{\boldsymbol{O}} \left\{ \frac{1}{2\boldsymbol{\tau}} \|\boldsymbol{B} - \boldsymbol{IO}\|_2^2 + \|\boldsymbol{\phi O}\|_1 \right\}, \tag{3}$$

where τ is a regularization parameter. Here, we describe $\boldsymbol{\phi O} = \boldsymbol{v}$, and (3) can be expressed as

$$\min_{v} \left\{ \frac{1}{2\boldsymbol{\tau}} \left\| \boldsymbol{B} - \boldsymbol{I\phi}^{-1}\boldsymbol{v} \right\|_2^2 + \|\boldsymbol{v}\|_1 \right\}. \tag{4}$$

b: TVCS [26]

TVCS is a CS algorithm that uses the property that the gradient of adjacent pixels ensures sparsity while effectively preserving the edge information by minimizing the TV of images. The gradient of images is the differential of adjacent pixel values because images are 2D discrete functions. TVCS is a minimization problem that replaces the l_1 norm of (3) with the l_1 norm of TV. The TV norm of image $\boldsymbol{O}$ is denoted as $\|\boldsymbol{O}\|_{\mathrm{TV}}$, and is written as

$$\begin{aligned} \|\boldsymbol{O}\|_{\mathrm{TV}} &= \|\mathrm{TV}(\boldsymbol{O})\|_1 \\ &= \sum_{i=1}^{m-1} \sum_{j=1}^{n-1} \sqrt{(o_{i+1,j} - o_{i,j})^2 + (o_{i,j+1} - o_{i,j})^2}, \end{aligned} \tag{5}$$

where $o_{i,j}$ is the pixel value at coordinate (i, j). The minimization problem of the TVCS is as follows:

$$\min_{\boldsymbol{O}} \left\{ \frac{1}{2\tau} \|\boldsymbol{B} - \boldsymbol{IO}\|_2^2 + \|\boldsymbol{O}\|_{\mathrm{TV}} \right\}. \tag{6}$$

c: LRCS [27], [28]

Natural images have self-similarity (the rows or columns of the image look alike, or patches are similar to other nonlocal structures within an entire image), which can be expressed by a low-rank prior. The matrix stacks similar patch vectors of the same image are low-rank and have sparse singular values. Using the nuclear norm, the minimization problem of the LRCS can be written as

$$\min_{\boldsymbol{O}} \left\{ \frac{1}{2\tau} \|\boldsymbol{B} - \boldsymbol{IO}\|_2^2 + \|\boldsymbol{O}\|_* \right\}, \tag{7}$$

where $\|\cdot\|_*$ represents the nuclear norm and is the sum of the singular values of the matrix.

2) IC METHOD [29], [30]

IC alternately repeats the regularization and denoising steps to obtain reconstructed images instead of solving the minimization problem, which we described in Section II-B1). The projected Landweber regularization is defined as

$$\boldsymbol{O}_t = \boldsymbol{O}_{t-1} + \alpha \boldsymbol{D}\boldsymbol{I}^{\mathrm{T}}(\boldsymbol{B} - \boldsymbol{I}\boldsymbol{O}_{t-1}), \quad t = 1, 2, 3, \cdots, \tag{8}$$

where $\boldsymbol{D}$ is a pseudo-inverse matrix of $\boldsymbol{I}^{\mathrm{T}}\boldsymbol{I}$, α is the gain factor to control the convergence speed, $\boldsymbol{O}_t$ is the approximate solution of (2), and $\boldsymbol{O}_{t-1}$ is an approximate solution to the previous equation. Here, the initial supposition is $\boldsymbol{O}_0 = [0, 0, \cdots, 0]^{\mathrm{T}}$.

After projected Landweber regularization, undersampling noise still exists in the approximate image. To remove noise, $\boldsymbol{O}_t$ is processed using a guided filter. The filtered image is denoted as

$$\boldsymbol{q}_t = \mathrm{guidedfilter}(\boldsymbol{P}_t, \boldsymbol{O}_t), \quad t = 1, 2, 3, \cdots, \tag{9}$$

where $\boldsymbol{P}_t$ is the guidance image ($t = 1, \boldsymbol{P}_t = \boldsymbol{O}_1, t > 1 : \boldsymbol{P}_t = \boldsymbol{q}_{t-1}$). The filtering output at pixel i is expressed as a weighted average

$$\boldsymbol{q}_{ti} = \sum_j W_{i,j}(\boldsymbol{P}_t)\boldsymbol{O}_{t,j}, \tag{10}$$

where i and j are pixel indexes. The filter kernel $W_{i,j}$ is a function of guidance image $\boldsymbol{I}$ and is independent of $\boldsymbol{O}$, which is defined as follows:

$$W_{i,j}(P) = \frac{1}{|\omega|^2} \sum_{k:(i,j)\in\omega_k} \left[1 + \frac{(O'_i - \mu_k)(O'_j - \mu_k)}{(\sigma_k^2 + \varepsilon)} \right], \tag{11}$$

where O' is the coordinate of the pixel value, ω_k is the k-th kernel function window, $|\omega|$ is the number of pixels in ω_k, ε is a regularization parameter, and μ_k and σ_k^2 are the mean and variance of $\boldsymbol{O}$ in ω_k, respectively.

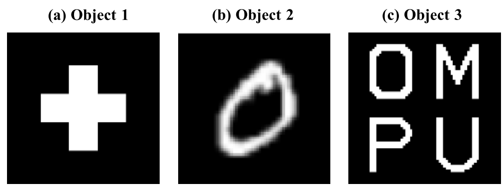

FIGURE 1. Target objects.

III. SIMULATION SETUP

A. TARGET OBJECTS

Three target objects were used, as shown in Fig. 1. Figures 1(a) and (c) present self-made images, and Fig. 1(b) shows one of the images from the MNIST [31].

The image size of all the target objects was 64 × 64 pixels. To discuss the system performance and complexity of the objects, we applied the local entropy of the images [32]. The entropy H in a window is defined as

$$H = -\sum_{i=0}^{k-1} U_i \log_2(U_i), \tag{12}$$

where U_i is the number of level i pixels in a window divided by the total number of pixels in the window. The entropy of the entire image is the average of all local entropies. The higher the entropy value, the more complex is the image.

Because the entropy of the images increases with the bit depth, we transformed the bit depth of object 2, which is grayscale, into 1 bit (binary). When the window size was 4 × 4, the entropies of objects 1–3 were 0.064, 0.119, and 0.132, respectively, and the three objects had different complexities. To evaluate the features of MCF-SPI system, these simple objects, which can be reconstructed sufficiently by MCF patterns, were mainly used. Reconstruction results for more complex objects are shown in section IV-D.

B. CORE LAYOUT OF MCFs AND MCF PATTERNS

This study compared 7-core, 14-core, and 21-core MCFs in the simulation. The 7-core MCF was designed and developed to achieve long-distance transmission [33], and the same core layout was used in previous research [16]. The complexity and variations of MCF patterns change significantly with the core layout. To quantitatively evaluate the complexity change of MCF patterns and pattern variations with core layout changes and select an appropriate layout, the entropy, rank, and correlation coefficient were introduced. We employed local entropy to compare the complexities of the MCF patterns quantitatively. Here, the bit depth was 4, the window size was 4 × 4, and we calculated the average of 1000 patterns. Pattern variation can be estimated by the rank of the pattern matrix $\boldsymbol{I}$ in the case of no noise. The average of correlation coefficient (C. C.), used for evaluating the randomness of patterns, of 1000 patterns were also calculated. Based on the results of our preliminary investigation of entropy H, rank R, and C. C. for 14-core and 21-core MCFs with several types of core placement, we selected the core

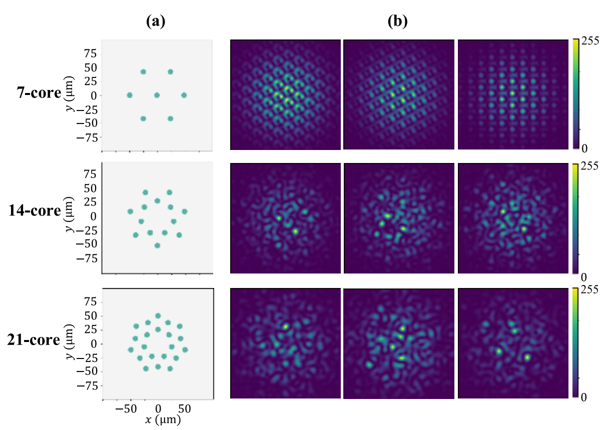

FIGURE 2. Designed MCFs and their pattern examples. (a) 7-core, 14-core, and 21-core MCFs. (b) Patten examples generated by each MCF.

TABLE 1. Entropy and rank of MCF patterns.

	7-core	14-core	21-core
Entropy	1.017	1.565	1.424
Rank	19	183	421
C. C.	0.213	0.150	0.148

placements (Figure 2(a)) with the highest ranks shown in Table 1. Figure 2 shows the MCFs that we designed and their pattern examples, and Table 1 lists the entropy, rank, and C.C. of each MCF pattern.

Here, the cladding diameter was 125 μm, and we assumed that there was no crosstalk. The wavelength of the input light was 1550 nm, the propagation mode of each core was a single mode, and the mode-field diameter was 10 μm. Figure 2(b) shows pattern examples generated by each MCF. The MCF patterns can be obtained using the Fraunhofer diffraction calculation of the light intensity and phase distribution at the MCF end face. We assumed that the patterns could be modulated by a random phase shift of light in each core. We also used 64 $\times$ 64 random binary patterns, which are generally applied in SPI.

1) ILLUMINATION AREA OF MCF PATTERNS

The light emitted by an MCF diverges with the distance from the end surface of the MCF to the object. Therefore, the pattern area illuminated on the target object changes with distance when the object size is maintained. The reconstructed image quality could differ, even if we used the same MCF core layout. Hence, we investigated the appropriate distance and illumination area for each MCF. For an object size of 5 mm $\times$ 5 mm and wavelength of 1550 nm, z is 165.2 mm for 7-core, 38.9 mm for 14-core, 24.5 mm for 21-core. The relationship between the propagation distance z and spread of pattern for Fraunhofer diffraction calculation based on FFT is expressed as follows:

$$z = \frac{Qs}{\lambda}, \tag{13}$$

where Q is the calculation width of the MCF end surface, s is the pixel pitch of pattern at the target object plane, and λ is the wavelength of the input light. To unify the size and number of pixels of the object and make the number of pixels of all MCF patterns equal to that of pixels of the object, we generated MCF patterns with a resolution of 64×64 pixels by changing the value of Q based on the equation (13) for each MCF core layouts by zero-padding in the simulation.

C. EVALUATION METRICS OF RECONSTRUCTED IMAGES

For quantitative evaluation of the reconstructed images, we used the peak signal to noise ratio (PSNR) as the metric [34]. The PSNR is defined as PSNR $= 10\log_{10}(\text{MAX}^2/\text{MSE})$, where MAX and MSE are the maximum possible pixel value of the image and mean squared error, respectively. Notably, there could be a discrepancy between the apparent quality of the reconstructed images and the PSNR values.

IV. SIMULATION RESULTS AND DISCUSSION

A. RECONSTRUCTION UNDER IDEAL CONDITIONS

First, we compared the reconstruction quality under ideal conditions without measurement noise. We used CVXPY ver. 1.1.7, one of the Python modules, to solve the minimization problem of CS algorithms. Figure 3 shows the reconstructed images with 1000 samplings (as we can see from the rank of the MCF patterns, the image quality converges sufficiently with 1000 samplings). Seven-core MCF patterns cannot obtain sufficient information about the objects. The reconstruction quality of the 14-core MCF and 21-core MCF is almost the same for objects 1–3. For object 1, TVCS and IC are the best for the MCF patterns, whereas random patterns can perfectly reconstruct the object using either algorithm. For object 2, the image quality achieved using CS and LRCS is better than that obtained using TVCS and IC. TVCS and IC are unable to restore blurry-edge information. For object 3, TVCS has the best quality for all types of patterns, but we could obtain perfect reconstructed images for either algorithm if we set random binary patterns to sufficient sampling numbers. Therefore, it was confirmed that the algorithms compatible with MCF-SPI differ depending on the target object image. In almost all cases, TVCS is the best algorithm, although there are a few exceptions, such as object 2, which has blurred edge information.

B. SAMPLING RATE

To obtain images within a short measurement time, it is desirable to reduce the sampling number. In this section, we discuss the reconstruction quality with different sampling rates ($= M/N$, where M is the sampling number, and N is the number of pixels in each object). We prepared 2000 patterns for each type of illumination pattern and randomly extracted M patterns 15 times to obtain the average PSNR. The results are shown in Figure 4.

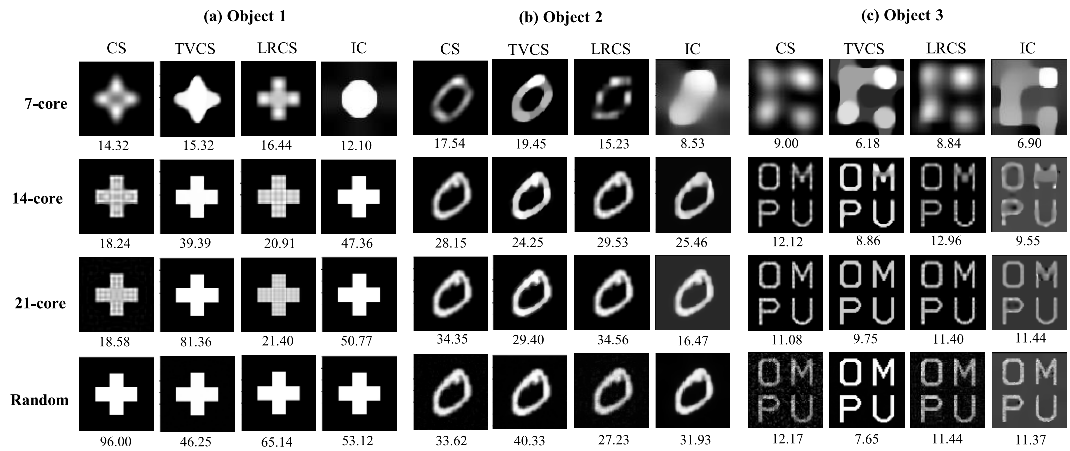

FIGURE 3. Reconstructed images and PSNRs under ideal conditions. Reconstructed images of object 1 (a), object 2 (b), and object 3 (c). The values under the reconstructed images are their PSNR values.

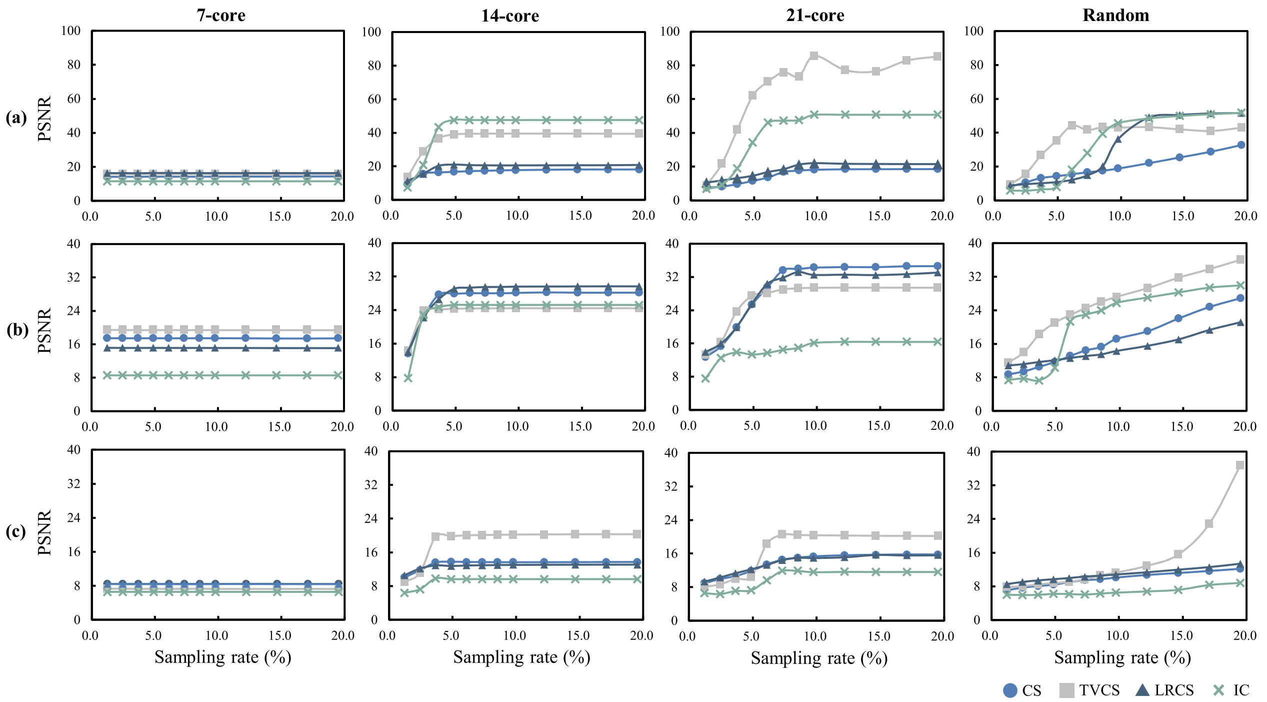

FIGURE 4. Quality of reconstructed images with different sampling rates. PSNR values of object (a) 1, (b) 2, and (c) 3 using four kinds of patterns with different sampling rates. Sampling rates are 0%–20%.

The results of the algorithm comparison are almost the same with different sampling rates. No algorithm is superior under low-sampling rate conditions. However, the higher the number of cores, the smaller is the sampling rate required for PSNR convergence. For example, for object 2, the sampling rate when the PSNR converges is approximately 5% for the 14-core MCF and approximately 7% for the 21-core MCF. As described in Section IV-A, objects 1 and 2 were perfectly reconstructed by compatible algorithms using a 14-core MCF. Because the 14-core MCF and 21-core MCF have almost the same entropy value, the rank of the 14-core MCF patterns is sufficient to obtain object information with an entropy of ~0.119. Therefore, we can reduce the sampling number and time using MCFs, in which the number of cores is limited to a certain degree. We can also reduce the cost by decreasing the number of cores because fewer modulators are needed. Moreover, the convergence speed of MCF patterns is overwhelmingly faster than that of random binary patterns, so MCF patterns have advantages in terms of sampling number and time for a simple object.

C. MEASUREMENT NOISE

In the aforementioned investigation, we assumed no measurement noise. However, there is always some noise in experimental imaging. Hence, we compared the reconstruction quality by assuming pseudo-noise. In this system, fiber bending, pattern fluctuations, and environmental light cause noise. Because noises result in the error between pattern

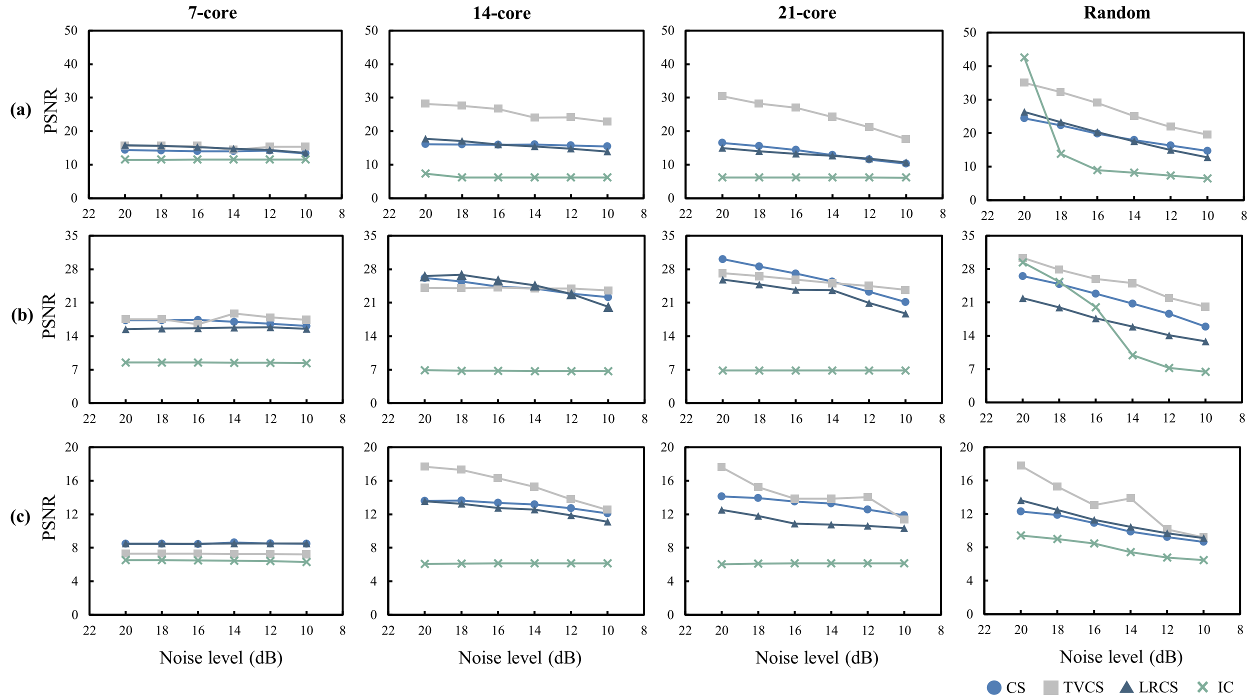

FIGURE 5. Quality of the reconstructed images with different noise levels. PSNR values of object (a) 1, (b) 2, and (c) 3 using four kinds of patterns with different noise levels. The noise level is 22–8 dB.

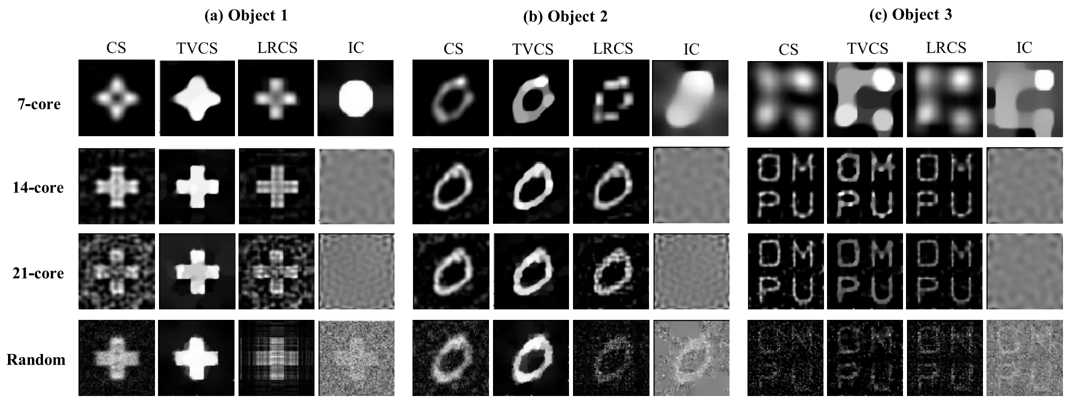

FIGURE 6. Reconstructed images with 10 dB noise. Reconstructed images of object 1 (a), object 2 (b), and object 3 (c).

matrix and light intensity matrix for solving the equation (2), we only consider the noise added to the intensity of the reflected light detected by a single-pixel detector. We assume Gaussian noise, with a probability distribution is defined as

$$N(x) = \frac{1}{\sqrt{2\pi}\sigma} \exp(-\frac{(x-\mu)^2}{2\sigma^2}), \qquad (14)$$

where μ is the average and σ is the standard deviation. Random data obtained with a Gaussian distribution were treated as percentages of the light intensity. We defined the noise level as $10\log_{10}(\overline{B}/3\sigma)$ dB, where $\overline{B}$ is the average light intensity. Figure 5 shows the quality of the reconstructed images with different noise levels, and Figure 6 presents the reconstructed images at a noise level of 10 dB. Here, the sampling rate is 24%.

In the MCF patterns, the slope of the PSNR with all noise levels is similar, and no algorithms are superior when measurement noise is added. Regardless of the noise level, the compatibility between the objects and algorithms determines the quality of the reconstructed images. However, the images reconstructed using IC are deteriorated significantly, even at a low noise level. IC and TVCS show almost the same reconstruction quality under ideal conditions, but TVCS is superior if measurement noise is considered. Similar to the sampling rate results, the slope of PSNR increases as the number of cores increases. The larger the entropy and rank values, the more information the MCF patterns can obtain about the, but the sensitivity to noise also increases. The results demonstrate that the reconstruction quality with measurement noise increases when using MCFs, and the number of cores is limited to a certain degree if the object entropy is approximately 0.119.

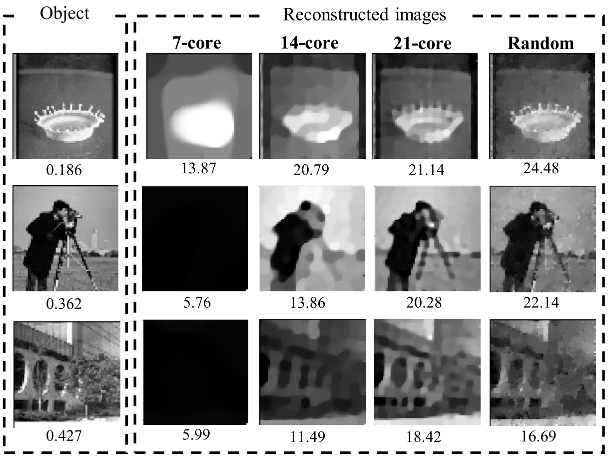

FIGURE 7. Reconstructed images of the complex objects. The numbers under the objects are the entropy values, and the figures under the reconstructed images are the PSNRs.

D. RECONSTRUCTION OF COMPLEX IMAGES

We investigated the reconstruction quality of complex images to evaluate the imaging performance of MCF patterns in more realistic scenes. We used TVCS, which was superior to the other algorithms in the above simulations. Figure 7 shows the reconstructed images with 24% sampling rate.

As shown in Fig. 7, the image quality of the 21-core MCF is superior to that of the 14-core MCF when the object is complex. The rank of the 14-core MCF is too small to obtain sufficient information about the objects; the entropy is greater than approximately 0.186. The reconstruction quality is improved because of the increase in rank as the number of cores increases. Notably, the number of cores must be increased to reconstruct complex objects completely, and the cladding diameter will be more extensive with an increasing number of cores.

V. CONCLUSION

We investigated the features and properties of speckle patterns generated by MCFs. Furthermore, we investigated reconstruction algorithms that are compatible with the SPI system. From the results of numerical simulations under ideal conditions without noise, different sampling rates, and measurement noise, TVCS is the most suitable algorithm for the system. However, TVCS is weak in restoring blurry-edge information. The entropy and rank of the MCF patterns differ depending on the number and placement of cores. For simple objects with an entropy of ∼0.119, MCF patterns have an entropy of approximately 1.5, and a rank of 183 can provide sufficient information about the objects. However, MCF patterns cannot obtain sufficient information even if a 21-core MCF is used when the entropy of the objects exceeds approximately 0.186. In conclusion, this study demonstrated that MCF-SPI has the potential to improve the measurement time and noise robustness compared to SPI using random binary patterns if a suitable core layout for the complexity of the target objects and application is set. This study provides information that can be used to reduce the system size of SPI effectively while maintaining sufficient image reconstruction quality.

REFERENCES

[1] J. H. Shapiro, "Computational ghost imaging," *Phys. Rev. A, Gen. Phys.*, vol. 78, no. 6, Dec. 2008, Art. no. 061802, doi: 10.1103/PhysRevA.78.061802.

[2] L. Bian, J. Suo, G. Situ, Z. Li, J. Fan, F. Chen, and Q. Dai, "Multispectral imaging using a single bucket detector," *Sci. Rep.*, vol. 6, p. 24752, 2016, doi: 10.1038/srep24752.

[3] S. S. Welsh, M. P. Edgar, R. Bowman, P. Jonathan, B. Sun, and M. J. Padgett, "Fast full-color computational imaging with single-pixel detectors," *Opt. Exp.*, vol. 21, no. 20, pp. 23068–23074, 2013, doi: 10.1364/OE.21.023068.

[4] H. Yu, R. Lu, S. Han, H. Xie, G. Du, T. Xiao, and D. Zhu, "Fourier-transform ghost imaging with hard X-rays," *Phys. Rev. Lett.*, vol. 117, no. 11, 2016, Art. no. 113901, doi: 10.1103/PhysRevLett.117.113901.

[5] A.-X. Zhang, Y.-H. He, L.-A. Wu, L.-M. Chen, and B.-B. Wang, "Tabletop X-ray ghost imaging with ultra-low radiation," *Optica*, vol. 5, no. 4, pp. 374–377, 2018, doi: 10.1364/OPTICA.5.000374.

[6] W. L. Chan, K. Charan, D. Takhar, K. F. Kelly, R. G. Baraniuk, and D. M. Mittleman, "A single-pixel terahertz imaging system based on compressed sensing," *Appl. Phys. Lett.*, vol. 93, no. 12, 2018, Art. no. 121105, doi: 10.1063/1.2989126.

[7] D. Shrekenhamer, C. M. Watts, and W. J. Padilla, "Terahertz single pixel imaging with an optically controlled dynamic spatial light modulator," *Opt. Exp.*, vol. 21, no. 10, pp. 12507–12518, 2013, doi: 10.1364/OE.21.012507.

[8] B. Sun, M. P. Edgar, R. Bowman, L. E. Vittert, S. Welsh, A. Bowman, and M. J. Padgett, "3D computational imaging with single-pixel detectors," *Science*, vol. 340, no. 6134, pp. 844–847, May 2013, doi: 10.1126/science.1234454.

[9] Z. Zhang and J. Zhong, "Three-dimensional single-pixel imaging with far fewer measurements than effective image pixels," *Opt. Lett.*, vol. 41, no. 11, pp. 2497–2500, 2016, doi: 10.1364/OL.41.002497.

[10] M. Le, G. Wang, H. Zheng, J. Liu, Y. Zhou, and Z. Xu, "Underwater computational ghost imaging," *Opt. Exp.*, vol. 25, no. 19, pp. 22859–22868, 2017, doi: 10.1364/OE.25.022859.

[11] X. Yang, Y. Liu, X. Y. Mou, T. Y. Hu, F. Yuan, and E. Cheng, "Imaging in turbid water based on a Hadamard single-pixel imaging system," *Opt. Exp.*, vol. 29, no. 8, pp. 12010–12023, Apr. 2021, doi: 10.1364/OE.421937.

[12] P. Clemente, V. Durán, V. Torres-Company, E. Tajahuerce, and J. Lancis, "Optical encryption based on computational ghost imaging," *Opt. Lett.*, vol. 35, no. 14, pp. 2391–2393, Jul. 2010, doi: 10.1364/OL.35.002391.

[13] M. Tanha, R. Kheradmand, and S. A. Kandjani, "Gray-scale and color optical encryption based on computational ghost imaging," *Appl. Phys. Lett.*, vol. 101, no. 10, 2012, Art. no. 101108, doi: 10.1063/1.4748875.

[14] R. N. Mahalati, R. Y. Gu, and J. M. Kahn, "Resolution limits for imaging through multi-mode fiber," *Opt. Exp.*, vol. 21, no. 2, pp. 1656–1668, 2013.

[15] C. Liu, J. Chen, J. Liu, and X. Han, "High frame-rate computational ghost imaging system using an optical fiber phased array and a low-pixel APD array," *Opt. Exp.*, vol. 26, no. 8, pp. 10048–10064, 2018, doi: 10.1364/OE.26.010048.

[16] K. Ikeda, Y. Kameyama, O. Koyama, and M. Yamada, "Imaging using single-pixel detector and multicore fiber," in *Imag. Appl. Opt. Congr., OSA Tech. Dig.* Optica Publishing Group, 2020, Paper DF1A.2.

[17] B. J. Puttnam, G. Rademacher, and R. S. Luis, "Space-division multiplexing for optical fiber communications," *Optica*, vol. 8, no. 9, pp. 1186–1203, Sep. 2021, doi: 10.1364/OPTICA.427631.

[18] G. M. Saridis, D. Alexandropoulos, G. Zervas, and D. Simeonidou, "Survey and evaluation of space division multiplexing: From technologies to optical networks," *IEEE Commun. Surveys Tuts.*, vol. 17, no. 4, pp. 2136–2156, 4th Quart., 2015, doi: 10.1109/COMST.2015.2466458.

[19] K. Ikeda, Y. Kameyama, O. Koyama, and M. Yamada, "Experimental demonstration of single-pixel imaging using a multi-core fibre," *Electron. Lett.*, vol. 57, no. 15, pp. 582–583, Jul. 2021, doi: 10.1049/ell2.12200.

[20] Y. Tian, Z. Ding, H. Feng, R. Zhu, Y. Chen, F. Xu, and Y. Lu, "Single-pixel imaging based on optical fibers," *IEEE Photon. J.*, vol. 12, no. 6, pp. 1–7, Dec. 2020, doi: 10.1109/JPHOT.2020.3035242.

[21] L. H. Bian, J. L. Suo, Q. H. Dai, and F. Chen, "Experimental comparison of single-pixel imaging algorithms," *J. Opt. Soc. Amer. A, Opt. Image Sci.*, vol. 35, no. 1, pp. 78–87, Jan. 2018, doi: 10.1364/JOSAA.35.000078.

[22] E. J. Candes and M. B. Wakin, "An introduction to compressive sampling," *IEEE Signal Process. Mag.*, vol. 25, no. 2, pp. 21–30, Mar. 2008, doi: 10.1109/MSP.2007.914731.

[23] R. G. Baraniuk, V. Cevher, M. F. Duarte, and C. Hegde, "Model-based compressive sensing," *IEEE Trans. Inf. Theory*, vol. 56, no. 4, pp. 1982–2001, Apr. 2010, doi: 10.1109/TIT.2010.2040894.

[24] O. Katz, Y. Bromberg, and Y. Silberberg, "Compressive ghost imaging," *Appl. Phys. Lett.*, vol. 95, no. 13, Sep. 2009, Art. no. 131110, doi: 10.1063/1.3238296.

[25] M. F. Duarte, M. A. Davenport, D. Takhar, J. N. Laska, T. Sun, K. F. Kelly, and R. G. Baraniuk, "Single-pixel imaging via compressive sampling," *IEEE Signal Process. Mag.*, vol. 25, no. 2, pp. 83–91, Mar. 2008, doi: 10.1109/MSP.2007.914730.

[26] R. Zhu, G. Li, and Y. Guo, "Compressed-sensing-based gradient reconstruction for ghost imaging," *Int. J. Theor. Phys.*, vol. 58, no. 4, pp. 1215–1226, Apr. 2019, doi: 10.1007/s10773-019-04013-x.

[27] H. Huang, C. Zhou, W. Gong, and L. Song, "Block matching low-rank for ghost imaging," *Opt. Exp.*, vol. 27, no. 26, pp. 38624–38634, 2019, doi: 10.1364/OE.27.038624.

[28] D. Yang, M. Hao, G. Wu, C. Chang, B. Luo, and L. Yin, "Single multimode fiber imaging based on low-rank recovery," *Opt. Lasers Eng.*, vol. 149, Feb. 2022, Art. no. 106827, doi: 10.1016/j.optlaseng.2021.106827.

[29] H. Huang, C. Zhou, T. Tian, D. Liu, and L. Song, "High-quality compressive ghost imaging," *Opt. Commun.*, vol. 412, pp. 60–65, Apr. 2018, doi: 10.1016/j.optcom.2017.12.010.

[30] C. Zhou, G. Wang, H. Huang, L. Song, and K. Xue, "Edge detection based on joint iteration ghost imaging," *Opt. Exp.*, vol. 27, no. 19, pp. 27295–27307, 2019, doi: 10.1364/OE.27.027295.

[31] Y. Lecun, L. Bottou, Y. Bengio, and P. Haffner, "Gradient-based learning applied to document recognition," *Proc. IEEE*, vol. 86, no. 11, pp. 2278–2324, Nov. 1998, doi: 10.1109/5.726791.

[32] C. Yan, N. Sang, and T. Zhang, "Local entropy-based transition region extraction and thresholding," *Pattern Recog. Lett.*, vol. 24, no. 16, pp. 2935–2941, 2003, doi: 10.1016/S0167-8655(03)00154-5.

[33] B. Zhu, T. F. Taunay, M. Yan, J. M. Fini, M. Fishteyn, E. M. Monberg, and F. V. Dimarcello, "Seven-core multi-core fiber transmissions for passive optical network," *Opt. Exp.*, vol. 18, no. 11, pp. 11117–11122, 2010, doi: 10.1364/OE.18.011117.

[34] A. Horé and D. Ziou, "Image quality metrics: PSNR vs. SSIM," in *Proc. 20th Int. Conf. Pattern Recognit.*, Aug. 2010, pp. 2366–2369, doi: 10.1109/ICPR.2010.579.

RYUTA YAMAGUCHI received the B.E. degree from Osaka Prefecture University (OPU), Japan, in 2021, where he is currently pursuing the master's degree in engineering. His research interest includes single-pixel imaging systems using optical fibers.

KANAMI IKEDA received the Ph.D. degree in engineering from the University of Electro-Communications, Japan, in 2018. She is currently an Associate Professor with the Graduate School of Engineering, Division of Electrical and Electronic Engineering, Osaka Metropolitan University, Japan. Her research interests include optical information processing and optical sensing.

OSANORI KOYAMA (Member, IEEE) received the B.E., M.E., and Ph.D. degrees from Osaka Prefecture University, Japan, in 1999, 2001, and 2013, respectively. He is currently an Associate Professor with the Photonic Innovative Systems Research Group, Osaka Metropolitan University. His research interests include design and control issues related to optical IP networks based on software defined networking and optical fiber sensing systems over IP networks.

MAKOTO YAMADA (Senior Member, IEEE) received the B.E. and M.E. degrees in electrical engineering from the Technical University of Nagaoka, Niigata, Japan, in 1983 and 1985, respectively, and the D.E. degree in optical amplifiers, in 1999.

He joined NTT Laboratories in 1985, where he was engaged in research on planar lightwave circuits. Since 1989, he has been engaged in research on optical fiber amplifiers. He joined Osaka Prefecture University, in 2008, where he has been a Professor, since 2013. He is currently a Professor with the Graduate School of Engineering, Osaka Metropolitan University, Japan. His research interests include design and control for optical amplifiers and other components in optical networks. He is a member of the Japan Society of Applied Physics and a fellow of the Institute of Electronics, Information and Communication Engineers of Japan (IEICE) and the Optical Society (OSA). He received the Paper Award from the IEICE, in 1994; the *Electronics Letters* Premium from the Institution of Electrical Engineers, in 1997; and the Sakurai Prize and Meritorious Award of 40th Foundation Anniversary from the Optoelectronics Industry and Technology Development Association, in 1998 and 2021, respectively.